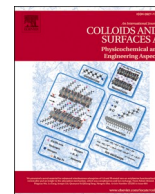




Contents lists available at ScienceDirect

Colloids and Surfaces A: Physicochemical and Engineering Aspects

journal homepage: www.elsevier.com/locate/colsurfa

ZnO/NiO heterostructures with enhanced photocatalytic activity obtained by ultrasonic spraying of a NiO shell onto ZnO nanorods

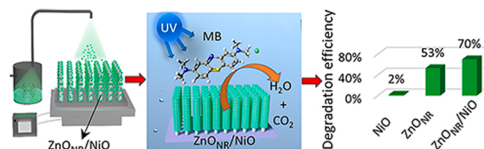
Zengjun Chen^a, Tatjana Dedova^a, Nicolae Spalatu^a, Natalia Maticiu^b, Marin Rusu^c,
Atanas Katerski^a, Ilona Oja Acik^a, Thomas Unold^c, Malle Krunk^{a,*}

^a Laboratory of Thin Films Chemical Technologies, Department of Materials and Environmental Technology, Tallinn University of Technology, Ehitajate tee 5, 19086 Tallinn, Estonia

^b Competence Centre Photovoltaics Berlin (PVcomB), Helmholtz-Zentrum Berlin für Materialien und Energie (HZB), Schwarzschildstraße 3, 12489 Berlin, Germany

^c Struktur und Dynamik von Energiematerialien, Helmholtz-Zentrum Berlin für Materialien und Energie, Lise-Meitner Campus, Hahn-Meitner-Platz 1, 14109 Berlin, Germany

GRAPHICAL ABSTRACT



ARTICLE INFO

Keywords:

NiO film
Ultrasonic spray
n-ZnO/p-NiO photocatalyst
n-ZnO/p-NiO band diagram
Methylene blue
Photocatalytic degradation

ABSTRACT

Degradation of organic pollutants such as methylene blue (MB) from water resources is currently of particular interest. Employment of a heterojunction device with optimized layer properties and proper interface engineering can enhance the photocatalytic performance by taking advantage of efficient charge separation. In this work, we develop an efficient photocatalytic system for the MB degradation based on ZnO nanorod (ZnONR)/NiO core-shell heterostructure with an optimized chemical and electronic structure for achieving record MB degradation efficiency of ~70%. ZnONR were grown by hydrothermal technique, whereas homogeneous crystalline NiO thin films were prepared by a robust and easy for up-scaling method of ultrasonic spray pyrolysis (USP). The optimum preparation conditions of photocatalytically efficient ZnONR/NiO heterostructures imply NiO film deposition from two USP cycles at 500 °C followed by air annealing heterostructures at 600 °C. The photocatalytic performance of ZnONR/NiO core-shell structure was investigated in comparison to counterpart layers and ZnO/NiO bilayer system. Chemical composition and band alignment at the ZnONR/NiO interface were investigated by X-ray photoelectron spectroscopy, Kelvin probe and photoelectron yield spectroscopy. Current transport studies indicated the presence of built-in electric field at the n-ZnO/p-NiO heterointerface responsible for the enhanced photocatalytic activity and based on this the degradation mechanism of MB is discussed.

* Correspondence to: Department of Materials and Environmental Technology, Tallinn University of Technology, Ehitajate tee 5, 19086 Tallinn, Estonia.

E-mail addresses: zengjun.chen@taltech.ee (Z. Chen), tatjana.dedova@taltech.ee (T. Dedova), nicolae.spalatu@taltech.ee (N. Spalatu), natalia.maticiu@helmholtz-berlin.de (N. Maticiu), rusu@helmholtz-berlin.de (M. Rusu), atanas.katerski@taltech.ee (A. Katerski), ilona.oja@taltech.ee (I.O. Acik), unold@helmholtz-berlin.de (T. Unold), malle.krunk@taltech.ee (M. Krunk).

<https://doi.org/10.1016/j.colsurfa.2022.129366>

Received 4 April 2022; Received in revised form 27 May 2022; Accepted 29 May 2022

Available online 31 May 2022

0927-7757/© 2022 The Author(s). Published by Elsevier B.V. This is an open access article under the CC BY-NC-ND license (<http://creativecommons.org/licenses/by-nc-nd/4.0/>).

1. Introduction

The removal of organic pollutants from water resources is currently of particular concern and photocatalysis is considered a prospective technology for the decomposition of organic pollutants [1]. Among various materials, ZnO is considered an excellent photocatalyst due to its suitable bandgap (~3.37 eV), high photocatalytic activity (PA), biocompatibility, and low cost [2]. It has been reported that ZnO is capable of degrading various organic pollutants, such as methylene blue (MB) [3], methyl orange [4], rhodamine B [5], and acridine orange [6]. However, one major drawback of ZnO as a photocatalyst is its complex point-defect structure, which promotes rapid recombination of photo-generated electron-hole pairs, inhibiting its PA [7–9] and retarding its practical application. One way to overcome this drawback is to couple ZnO with another semiconductor to form a heterojunction [10–14]. In a p-n heterojunction, photogenerated electron-hole pairs are separated by the gradients in their electrochemical potential and the asymmetric conductivity types in the n and p layers [12]. Therefore, a properly engineered heterojunction photocatalyst has the potential for higher PA because of the spatial separation of photogenerated electron-hole pairs. The most commonly used p-type metal oxide semiconductors to form a heterostructure with ZnO are Cu_xO [10,15–17] and NiO [11–13,18,19]. NiO has also been studied as a photocatalyst [20,21] due to its tunable bandgap (3.0–4.3 eV) [22], low material cost and high chemical stability. However, the PA of single NiO is much worse than that of ZnO. The higher PA of ZnO/NiO heterostructures than of either NiO or ZnO has been demonstrated in several studies [8,11–13,18,19,23–26].

In the majority of these studies, the ZnO/NiO photocatalyst was in powder form. For example, Thampy et al. [18] found that ZnO/NiO nanocomposites synthesized by the sonochemical route exhibited an MB degradation efficiency of 90 % in 1 h under sunlight irradiation, in contrast to efficiencies of 20 % and 40 % for degradation by NiO and ZnO alone, respectively. Tian et al. [13] reported that ZnO/NiO nanoparticles grown by precipitation in solution showed a methyl orange degradation efficiency of 100 % under UV illumination over 25 min, in contrast to efficiencies of 10 % and 40 % for NiO and ZnO, respectively. It was also reported that ZnO/NiO nanoparticles prepared by precipitation in solution had a rhodamine B degradation efficiency of 90 % in 200 min under UV light irradiation, in contrast to values of 20 % for NiO and 80 % for ZnO [19]. A photocatalytic degradation efficiency of ca. 80 % for binary mixture of rhodamine B and methylene blue was also reported employing ZnO-NiO composite nanofibers [24].

Although nanopowders and nanofibers obtained such a high degradation efficiency, these approaches have severe drawbacks, such as particle agglomeration and the difficulty of separating photocatalyst from wastewater, causing secondary pollution. The development of heterogeneous photocatalysts immobilized on a substrate, such as a bilayer or core-shell heterostructure, is a more promising approach that allows easy separation and recovery of photocatalysts from polluted environment [11,12]. ZnO nanorod (ZnO_{NR}) layers have been used in $\text{ZnO}_{\text{NR}}/\text{CuO}$ [10,27,28] and $\text{ZnO}_{\text{NR}}/\text{NiO}$ core-shell heterostructures [11, 12] and have the advantage of an increased active surface area compared thin films. For example, $\text{ZnO}_{\text{NR}}/\text{CuO}$ photocatalysts on a substrate, fabricated by solution methods exhibited a 85 % [27] and a 93 % [28] degradation efficiency of MB in 180 min under UV irradiation, being significantly higher than 50 % for ZnO. $\text{ZnO}_{\text{NR}}/\text{CuO}$ core shell structure with CuO by sputtering showed a 80 % methyl orange degradation efficiency in 240 min under UV light compared to ZnO_{NR} [10].

Unlike $\text{ZnO}_{\text{NR}}/\text{CuO}$ photocatalysts, photocatalytic performance of $\text{ZnO}_{\text{NR}}/\text{NiO}$ structures has been studied only in few reports [11,12], although ZnO-NiO nanocomposite photocatalysts in powder and nanofiber form posed high capability to degrade different pollutants. In this perspective, Periyannan et al. [11] reported that $\text{ZnO}_{\text{NR}}/\text{NiO}$ fabricated by sputtering NiO on ZnO_{NR} had a rhodamine B degradation efficiency of 58 % in 180 min under UV light irradiation, in contrast to 54 % for

ZnO_{NR} . Ding et al. [12] found that a ZnO/NiO hierarchical structure on carbon fiber cloth prepared by electrodeposition of NiO on ZnO exhibited a 95 % degradation efficiency of both rhodamine B and methylene orange in 180 min under UV light irradiation, in contrast to 35 % for NiO and 38 % for ZnO.

Although such approaches showed potential for high PA, there is still space for the development and optimization of ZnO/NiO heterojunction photocatalysts, to explore the full potential of this heterostructure. In particular, a specific focus should be set on the optimization of NiO shell properties. The effect of NiO shell thickness on the PA of $\text{ZnO}_{\text{NR}}/\text{NiO}$ core-shell heterostructures was observed in one publication [12] but has never been systematically studied. Moreover, only few methods such as sputtering [11] and electrodeposition [12] were applied to deposit NiO shell. However, the ultrasonic spray pyrolysis (USP) method, a simple and easy for up-scaling method that allows fabrication of thin films with good uniformity and controlled thickness [29–31], has not been used for NiO film deposition to form ZnO/NiO heterostructure until now.

In this study, we investigated the deposition of NiO films by USP and its application in ZnO/NiO core-shell heterostructure. Employment of such heterostructure with optimized NiO shell thickness and ZnO/NiO interface can enhance the photocatalytic performance by taking advantage of efficient charge separation. For NiO film deposition, the nickel acetylacetonate, that has been rarely used for NiO film deposition by spray method [32], was employed as a nickel source. The effect of NiO deposition temperature on the NiO film properties, ZnO/NiO bilayer heterostructure formation and PA for MB degradation was studied. Based on the results, the most suitable temperature for NiO shell deposition onto ZnO_{NR} was selected to optimize NiO shell thickness in the $\text{ZnO}_{\text{NR}}/\text{NiO}$ core-shell heterostructure. Characterization techniques of X-ray photoelectron spectroscopy (XPS), Kelvin probe (KP) analysis and photoelectron yield spectroscopy (PYS) were applied experimentally to prove the formation of n-p junction. As a proof of concept, we developed an efficient $\text{ZnO}_{\text{NR}}/\text{NiO}$ core-shell photocatalytic system with an optimized chemical and electronic structure, which allowed achieving a record MB degradation efficiency of ~70 %.

2. Experimental

2.1. Sample preparation

Three types of samples were prepared on borosilicate glass with a size of $25 \times 9 \times 1 \text{ mm}^3$: (i) NiO thin films, (ii) NiO films deposited onto ZnO films (ZnO/NiO bilayer heterostructures) and (iii) NiO films deposited on ZnO nanorods ($\text{ZnO}_{\text{NR}}/\text{NiO}$ core-shell heterostructures). The glass substrates were thoroughly precleaned with detergent solution, double deionized water, and ethanol in an ultrasonic bath.

2.1.1. Deposition of NiO films

NiO films were grown by the USP method at substrate temperatures (T_s) of 350, 400, 450, and 500 °C. Nickel acetylacetonate ($\text{Ni}(\text{C}_5\text{H}_7\text{O}_2)_2$, 96 %, Sigma-Aldrich Chemie GmbH, Germany) was used as the precursor to deposit NiO. The precursor was dissolved in ethanol to prepare a 10 mM solution. The air flow transporting precursor droplets from the nebulizer to the hot plate was set to 8 L/min. The spray rate was 4 mL/min, and the number of spray cycles was fixed at 12.

2.1.2. Deposition of ZnO films and ZnO nanorod layers

Zinc acetate dihydrate ($\text{Zn}(\text{CH}_3\text{COO})_2 \cdot 2\text{H}_2\text{O}$, 99.9 %, Sigma-Aldrich Chemie GmbH, Germany) was the precursor for the deposition of ZnO films as a component of the ZnO/NiO bilayer heterostructure and as a seed layer to grow ZnO nanorod layers (ZnO_{NR}). The precursor was dissolved in a mixture of water and isopropanol with a volume ratio of 2:3. The precursor concentration was 0.05 mol/L, and the volume of solution was 20 mL. A few drops of acetic acid were added to the zinc acetate solution to prevent hydrolysis of the precursor. The solution was nebulized with the help of a pneumatic sprayer, which operates in

pulsating mode (5 s spray, 20 s pause). The tin bath temperature was set to 450 °C, and an air flow of 6 L/min was used [33].

ZnO_{NR} was grown on a sprayed ZnO seed layer by a hydrothermal method [33]. Briefly, a glass substrate with a ZnO seed layer was placed into a reactor beaker that contained 40 mL of an aqueous solution of 0.1 mol/L zinc nitrate hexahydrate (Zn(NO₃)₂·6H₂O, 99.9 %, Sigma–Aldrich Chemie GmbH, Germany) and 0.1 mol/L hexamethylenetetramine ((CH₂)₆N₄). The reactor beaker was mounted in a steel autoclave, and the reaction was carried out at 120 °C for 2 h.

2.1.3. Preparation of ZnO/NiO heterostructures

To prepare ZnO/NiO bilayer heterostructures, a ZnO film was deposited first by pneumatic spraying, followed by deposition of a NiO film by USP at 350, 400, 450 and 500 °C. The corresponding ZnO/NiO bilayers were labeled ZnO/NiO(350), ZnO/NiO(400), ZnO/NiO(450), and ZnO/NiO(500). To keep the thickness of the NiO film similar when growing at different temperatures, the number of spray cycles was varied. We used 6, 4, 3, and 3 cycles for NiO grown at 350, 400, 450, and 500 °C, respectively.

To prepare ZnO_{NR}/NiO core-shell heterostructures, NiO films were deposited by USP onto hydrothermally grown ZnO_{NR} using 5 mM nickel acetylacetonate (Ni(acac)₂) in ethanol solution. The substrate temperature for NiO shell deposition was fixed to 500 °C. To vary the thickness of the NiO shell on ZnO_{NR}, 1, 2, and 4 cycles were used, and the corresponding ZnO_{NR}/NiO core-shell samples were labeled ZnO_{NR}/NiO(1), ZnO_{NR}/NiO(2), and ZnO_{NR}/NiO(4), respectively. A schematic illustration of the ZnO/NiO heterostructures is presented in Scheme 1.

A postdeposition annealing procedure was applied for all samples, including NiO films, ZnO_{NR} layers, ZnO/NiO bilayers and ZnO_{NR}/NiO core-shell heterostructures. Annealing was performed at temperature (T_{an}) of 600 °C for 1 h in air, and the samples were labeled accordingly. For example, ZnO_{NR}, ZnO_{NR}/NiO(2), and ZnO_{NR}/NiO(4) annealed at 600 °C were named ZnO_{NR}-600, ZnO_{NR}/NiO(2)-600, and ZnO_{NR}/NiO(4)-600, respectively.

2.2. Characterization methods

X-ray diffraction (XRD), scanning electron microscopy (SEM), and UV–VIS–NIR spectrophotometry were used to measure the XRD patterns, surface morphology and cross section, and total transmittance (T) and reflectance (R) spectra of the samples, respectively. The details on

the measurements and calculation of the optical parameters have been reported elsewhere [20].

The current-voltage (I-V) curves of the ZnO/NiO bilayer (NiO: T_s = 500 °C, 12 cycles) heterostructures on indium tin oxide (ITO) glass substrates were measured at room temperature in the dark by using a two-point probe method with an AutoLab PGSTAT-30. The contact material was graphite deposited from an aqueous graphite ink (Alfa Aesar).

The hot probe method in 2-contact configuration was used to determine the n-type or p-type conductivity of ZnO and NiO films.

The XPS spectra were measured with a standard XPS laboratory system based on a nonmonochromatic X-ray source from SPECS with a Mg anode providing an excitation energy of 1253.6 eV [34]. All XPS spectra were measured at room temperature at a pressure of 5×10^{-6} Pa. The energy analyzer was calibrated by fixing the C 1s binding energy at 285.0 eV.

KP and PYS analysis were used to measure the work function (Φ) and ionization energy (E_i) of the prepared samples, respectively, using a KP Technology SKP5050-APS02 instrument under ambient N₂ in the dark. The details of the measurements and calculation of the work function and ionization energy have been described elsewhere [35].

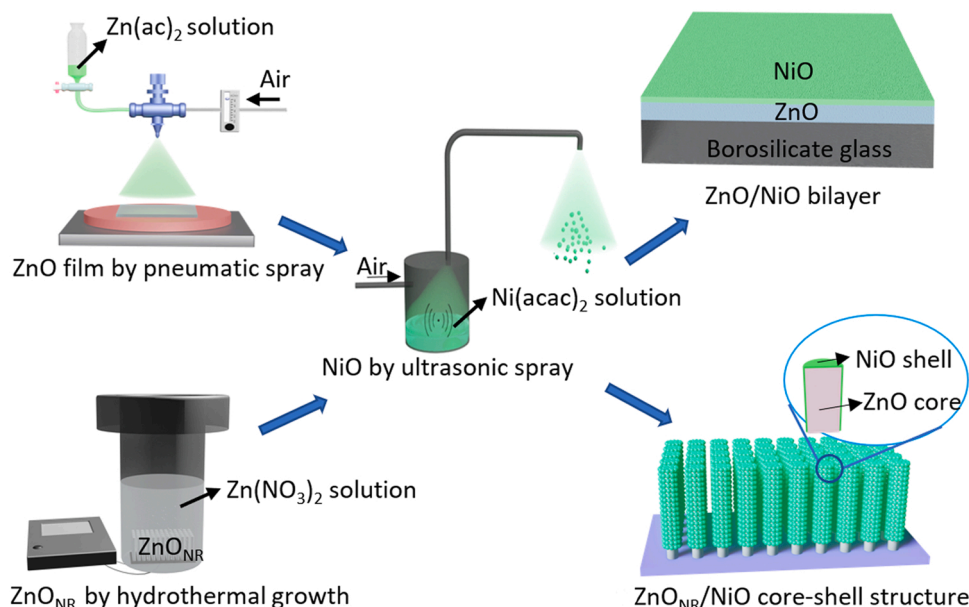
The photodegradation of MB dye was measured under UV-B irradiation (Philips, Hg, PL-L, 36 W, $\lambda_{\max} = 315$ nm) as described elsewhere [20]. Prior to the test, the samples were subjected to a cleaning procedure under UV-A irradiation (15 W, $\lambda_{\max} = 365$ nm) for 30 min. The initial concentration of MB aqueous solution (C₀) was set to 10 mg/L while keeping the volume at 2 mL. A Jasco V-670 UV–VIS–NIR spectrophotometer was used to measure the MB concentration at a given time (C) by recording the MB absorbance intensity at 660 nm. The absorbance spectra were recorded every 30 min for 3 h. The photodegradation efficiency of MB (η) was calculated according to Eq. (1) [20]:

$$\eta = (C_0 - C)/C_0 \times 100\% \quad (1)$$

The photodegradation kinetics of MB dye were estimated using the Langmuir-Hinshelwood model, and the reaction rate constant (k) was calculated from Eq. (2) [33]:

$$\ln(C_0/C) = kt \quad (2)$$

All the $\ln(C_0/C)$ vs. t curves follow a linear relationship with a correlation coefficient (R²) above 0.95, indicating that the



Scheme 1. Schematic illustration of the synthesis of ZnO/NiO heterostructures.

photodegradation of MB dye follows pseudo-first-order reaction kinetics. For each photodegradation measurement four samples, prepared under the same deposition conditions, were used. The standard deviations of degradation efficiencies were calculated.

To understand the role of different reactive species such as $\cdot\text{OH}$, $\cdot\text{O}_2^-$ and h^+ , in the photocatalytic degradation process, the photodegradation of MB in aqueous solution was measured by $\text{ZnO}_{\text{NR}}-600$ and $\text{ZnO}_{\text{NR}}/\text{NiO}(2)-600$ in the presence of tert-Butanol (t-BuOH) as $\cdot\text{OH}$ scavenger, p-Benzoquinone (p-BQ) as $\cdot\text{O}_2^-$ scavenger, and ammonium oxalate (AO) as h^+ scavenger, respectively. The concentration of scavengers in MB solution was set to 1 mmol/L. This measurement has been described elsewhere [36].

3. Results and discussion

3.1. NiO films prepared by USP: effect of growth temperature

First, we investigated the effects of USP deposition conditions on the properties of NiO films. XRD patterns of NiO films deposited at $T_s = 350\text{--}500\text{ }^\circ\text{C}$ are presented in Fig. 1a. The films showed a main reflection at $2\Theta = 43.51^\circ$, corresponding to the (200) plane of cubic NiO (PDF-2, 01-071-1179), while reflections corresponding to the (111) and (220) planes were less intense. The films exhibited preferential orientation of the crystallites along the (200) plane, as the intensity ratio of $I_{(200)}/I_{(111)}$ was in the range of 6–13, which is much higher than that of the powder reference of NiO ($I_{(200)}/I_{(111)} = 1.49$, PDF-2, 01-071-1179). The crystallite size of the NiO films deposited at $T_s = 350\text{--}500\text{ }^\circ\text{C}$ was calculated from the full width at half maximum (FWHM) of the (200) reflection using the Scherrer formula [20]. The values of crystallite size are presented in Table 1.

The crystallite size of NiO increased from 17 to 30 nm when T_s increased from 350 to 500 $^\circ\text{C}$. It is widely accepted that films deposited from acetylacetonate precursors may contain organic residuals, which can hinder crystallite growth. A classical procedure to remove organic residuals is postdeposition annealing in air at elevated temperatures in the range of 500–600 $^\circ\text{C}$ [37]. Thus, we applied air annealing at $T_{\text{an}} = 600\text{ }^\circ\text{C}$ for 1 h as the next step. Air annealing at $T_{\text{an}} = 600\text{ }^\circ\text{C}$

Table 1

Film thickness (d), crystallite size (D) and bandgap (E_g) of NiO films deposited onto glass substrates at $T_s = 350\text{--}500\text{ }^\circ\text{C}$ and after annealing at $T_{\text{an}} = 600\text{ }^\circ\text{C}$ for 1 h in air. All the samples were obtained from 10 mM $\text{Ni}(\text{acac})_2$ in ethanol solution using 12 spray cycles.

T_s ($^\circ\text{C}$)	d (nm)	D (nm)		E_g (eV)	
		As-dep	$T_{\text{an}} = 600\text{ }^\circ\text{C}$	As-dep	$T_{\text{an}} = 600\text{ }^\circ\text{C}$
350	30	17	24	3.8	3.7
400	45	22	25	3.7	3.7
450	60	25	30	3.7	3.7
500	70	30	30	3.7	3.7

resulted in a larger crystallite size of NiO films deposited at $T_s = 350\text{--}450\text{ }^\circ\text{C}$ (Table 1), while the crystallite size of NiO deposited at $T_s = 500\text{ }^\circ\text{C}$ remained the same at 30 nm after annealing.

The SEM images shown in Fig. 1c clearly demonstrate the uniformity and fine-grained structure of the sprayed NiO films independent of the deposition temperature. According to the SEM cross-sectional images, the film thickness increased from ca. 30 nm to ca. 70 nm when increasing T_s from 350 to 500 $^\circ\text{C}$ (Fig. 1c, Table 1). It is commonly observed that increasing the deposition temperature increases the thickness of metal oxide films (TiO_2 , ZrO_x) produced from acetylacetonate precursors by the spray method [29,31]. The total transmittance spectra of NiO films presented in Fig. 1b indicate an overall optical transmittance of 60–80 % in the visible spectral region. The transmittance of the films grown at lower temperature (350 $^\circ\text{C}$) was at least 10 % higher than the transmittance of the films deposited at 450 and 500 $^\circ\text{C}$. The lower optical transparency of NiO films deposited at higher temperatures is probably due to the larger film thickness (Table 1). As-prepared films deposited at 350 $^\circ\text{C}$ had an E_g of 3.8 eV. Increasing the deposition temperature from 400 to 500 $^\circ\text{C}$ led to similar E_g values of 3.7 eV. Independent of the growth temperature, all the films annealed at 600 $^\circ\text{C}$ showed a similar direct bandgap of 3.7 eV (Table 1). The higher E_g value of the NiO film grown at 350 $^\circ\text{C}$ could be explained by the presence of some residues in the film that are removed by annealing at 600 $^\circ\text{C}$.

In summary, it is confirmed for the first time that crystalline,

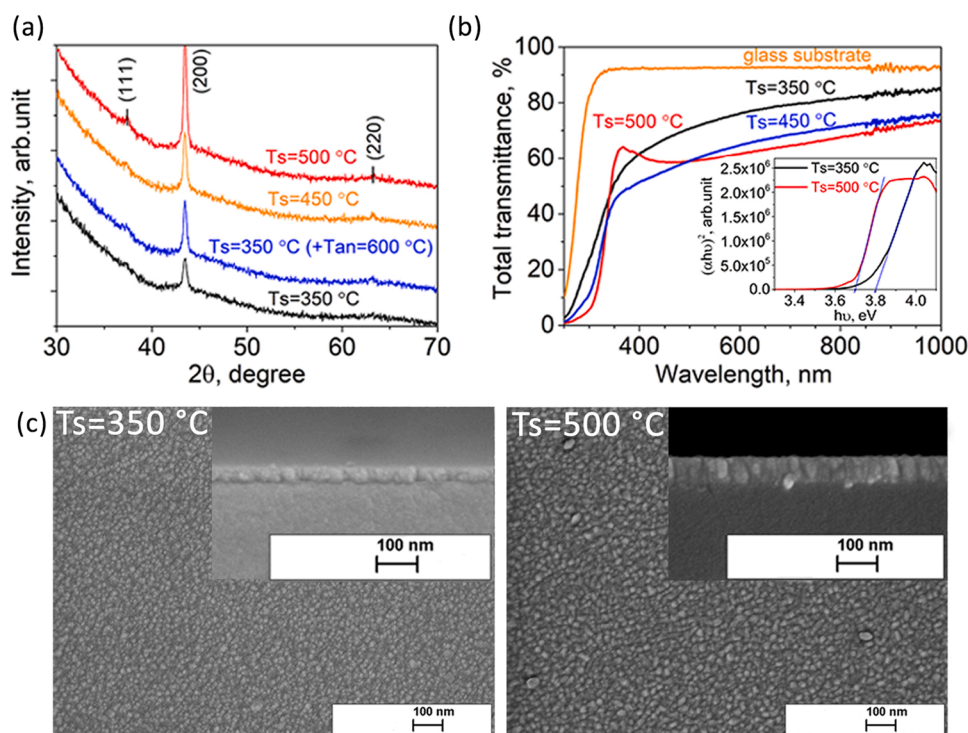


Fig. 1. (a) XRD patterns of NiO films deposited onto glass substrates at $T_s = 350\text{--}500\text{ }^\circ\text{C}$ and a NiO film deposited at $T_s = 350\text{ }^\circ\text{C}$ followed by annealing at $T_{\text{an}} = 600\text{ }^\circ\text{C}$ for 1 h in air. (b) Total transmittance spectra of NiO films deposited onto glass substrates at $T_s = 350\text{--}500\text{ }^\circ\text{C}$ (inset is the Tauc plot of NiO films deposited at 350 $^\circ\text{C}$ and 500 $^\circ\text{C}$). (c) SEM surface and cross-sectional images (inset) of NiO films deposited onto glass substrates at $T_s = 350\text{ }^\circ\text{C}$ and $T_s = 500\text{ }^\circ\text{C}$. All the samples were obtained from 10 mM $\text{Ni}(\text{acac})_2$ in ethanol solution using 12 spray cycles.

continuous NiO films with $E_g = 3.7$ eV can be successfully fabricated by the USP method using a nickel acetylacetonate precursor.

3.2. ZnO/NiO bilayer heterostructures: effect of NiO growth temperature

To study the effect of the NiO deposition temperature on the properties of ZnO/NiO bilayer heterostructures, NiO films were deposited onto ZnO at $T_s = 350$ – 500 °C. To keep the NiO film thickness similar at every deposition temperature, the number of spray cycles was varied; namely, 6, 4, 3 and 3 spray cycles at $T_s = 350$, 400, 450, and 500 °C, respectively, were applied.

XRD patterns of the NiO film and ZnO/NiO bilayer heterostructure with NiO deposited at $T_s = 500$ °C are presented in Fig. 2a. The diffractogram of the NiO film showed a reflection at 2θ of 43.56° corresponding to the (200) plane of NiO. For the ZnO/NiO bilayer heterostructure, the XRD pattern showed several reflections at 2θ of 31.79° , 34.48° , 36.36° , 47.67° , 63.04° , and 68.17° , corresponding to the (100), (002), (101), (102), (103), and (112) planes of ZnO, and at 2θ of 43.31° , corresponding to the (200) plane of NiO [18]. Thus, the XRD data confirmed that the NiO film was grown on the ZnO layer.

As a first attempt to prove the formation of a heterojunction between ZnO and NiO, the current-voltage characteristics were measured at room temperature. The current-voltage characteristics of the ZnO/NiO bilayer structure (Fig. 2b) showed pronounced rectifying behavior, indicating the formation of an n-p heterojunction. The conductivity type of each layer was measured by a hot probe, and the result indicated that the ZnO film is an n-type semiconductor material and the NiO film is a p-type semiconductor material.

To evaluate the photocatalytic performance of the as-deposited ZnO/NiO bilayer heterostructures as well as their constituent components, the NiO and ZnO films, MB dye degradation in aqueous solution under UV-B irradiation was measured and compared. The MB degradation curves of these samples are presented in Fig. 2c. The degradation efficiencies and degradation rate constant (k) values are summarized in Table 2.

As shown in Fig. 2c, independent of the deposition temperature, the NiO films possessed extremely low PA activity towards MB dye degradation, ca. 1 %. In the case of ZnO/NiO bilayer photocatalysts, PA varied greatly depending on the NiO deposition temperature. The higher the deposition temperature of NiO was, the higher the PA value was (Fig. 2c). The highest degradation efficiency of 30 % was achieved by the ZnO/NiO bilayer heterostructure with NiO grown at 500 °C (labeled ZnO/NiO(500) in Fig. 2c), in contrast to the value of 26 % for the ZnO film. Annealing at 600 °C improved the degradation efficiency of ZnO/NiO bilayer heterostructures when NiO was grown in the range of 350–450 °C, as presented in Table 2. However, no changes in degradation efficiency were observed for NiO grown at 500 °C.

Table 2

Degradation efficiencies of MB and degradation rate constants (k) obtained with as-deposited samples and samples annealed at $T_{an} = 600$ °C in air for 1 h: NiO films ($T_s = 350$ – 500 °C); ZnO film; and ZnO/NiO bilayer heterostructures with NiO grown at $T_s = 350$, 400, 450 and 500 °C. NiO was deposited from 10 mM Ni(acac)₂ in ethanol solution.

Sample	Degradation efficiency (%)		$k \times 10^{-3}$ (min ⁻¹)	
	As-dep	$T_{an} = 600$ °C	As-dep	$T_{an} = 600$ °C
NiO film	1	2	–	–
ZnO film	26	32	1.49	2.04
ZnO/NiO(350)	8	13	0.45	0.77
ZnO/NiO(400)	15	20	0.75	1.12
ZnO/NiO(450)	21	26	1.17	1.45
ZnO/NiO(500)	30	30	1.65	1.83

According to the MB photodegradation results, the ZnO/NiO bilayer heterostructure with NiO grown at $T_s = 500$ °C showed the highest degradation efficiency and rate, which also exceeded the PA of the ZnO as-grown film. Annealing of bilayer structures at 600 °C enhances the degradation efficiency compared to their untreated counterparts; however, no improvement in the PA of ZnO/NiO(500) bilayer heterostructures was observed. One possible reason for this phenomenon could be the unoptimized thickness of the NiO layer in the ZnO/NiO bilayer heterostructures. Thus, we further aimed to study the effect of NiO shell thickness on the PA of ZnO/NiO core-shell heterostructures, as will be discussed in the next section.

3.3. ZnO_{NR}/NiO core-shell heterostructures: effect of NiO shell thickness

To take advantage of the high surface active area of nanostructured layers [38], ZnO_{NR} was used as the building block for ZnO_{NR}/NiO core-shell heterostructures. The thickness of the NiO shell on ZnO_{NR} was varied by changing the number of spray cycles (1, 2, or 4 cycles). The deposition temperature of NiO was set at 500 °C according to the results obtained in Section 3.2.

SEM images of the surface of ZnO_{NR} and ZnO_{NR}/NiO core-shell heterostructures are presented in Fig. 3a. The ZnO_{NR} layers are composed of hexagonally shaped elongated ZnO crystals with an average diameter of ca. 100 nm. The ZnO_{NR}/NiO core-shell heterostructure produced from 10 mM Ni(acac)₂ solution with 2 spray cycles reveals coverage by ZnO_{NR} crystals with dots of fine-grained NiO. However, upon decreasing the concentration of Ni(acac)₂ solution from 10 mM to 5 mM, more uniform, denser and smoother coverage, hardly distinguishable on ZnO_{NR} (Fig. 3a), was formed. It should be added that no diffraction peaks characteristic of NiO were detected in the XRD pattern of the ZnO_{NR}/NiO core-shell heterostructure (Fig. S1). Thus, 5 mM Ni(acac)₂ solution was used to deposit NiO onto ZnO_{NR} to form a

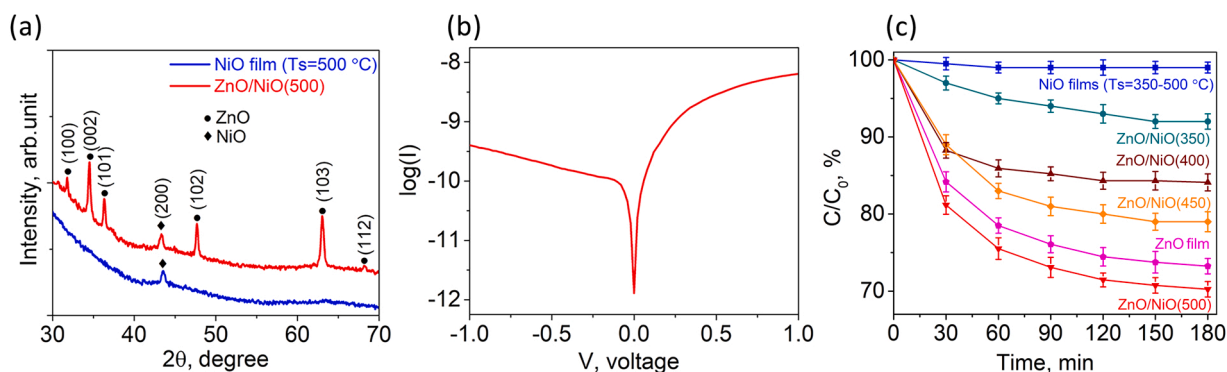


Fig. 2. (a) XRD patterns of NiO film deposited onto glass substrate at $T_s = 500$ °C and ZnO/NiO(500) bilayer heterostructure. (b) I-V curve of ZnO/NiO bilayer on ITO/glass (NiO was deposited at $T_s = 500$ °C using 12 spray cycles, ZnO/NiO bilayer was annealed at $T_{an} = 600$ °C for 1 h in air). (c) Degradation curves of MB by as-deposited samples under UV-B illumination: NiO films ($T_s = 350$ – 500 °C) on glass, ZnO film on glass, and ZnO/NiO(350), ZnO/NiO(400), ZnO/NiO(450), ZnO/NiO(500) bilayer heterostructures (number in bracket shows the NiO layer deposition temperature). NiO was deposited from 10 mM Ni(acac)₂ in ethanol solution.

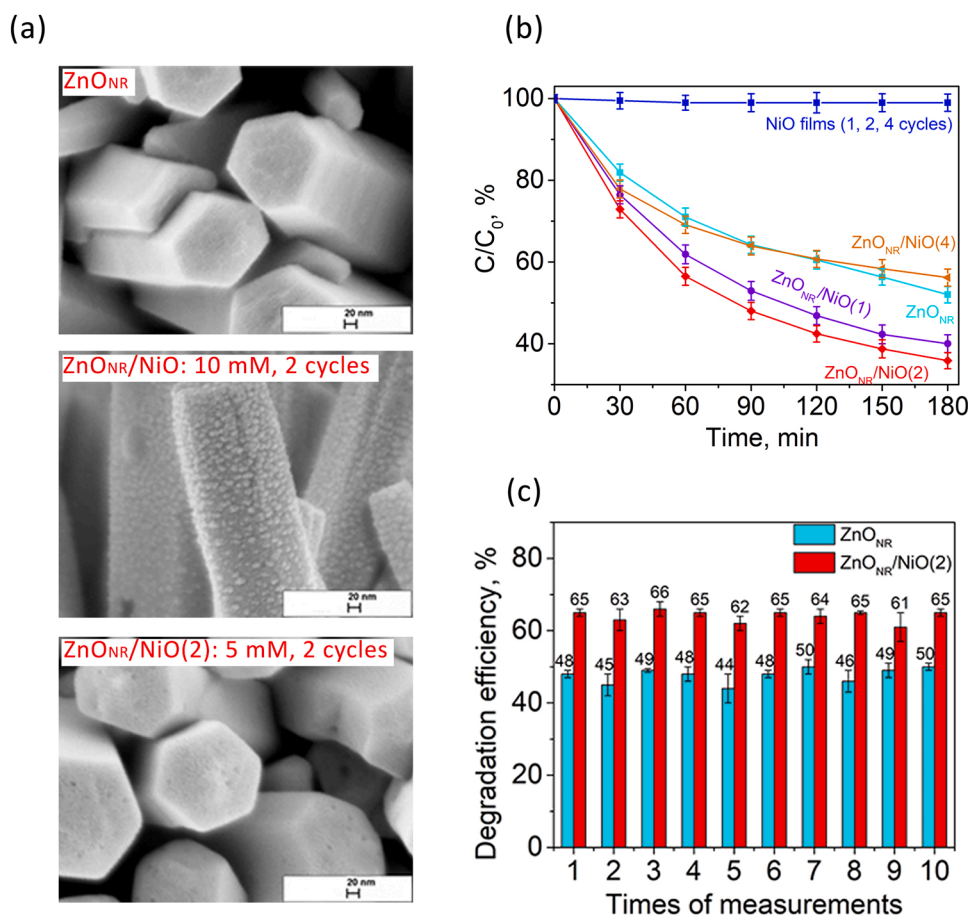


Fig. 3. (a) SEM images of ZnO_{NR} , $\text{ZnO}_{\text{NR}}/\text{NiO}$ core-shell heterostructures with NiO from 10 mM and 5 mM $\text{Ni}(\text{acac})_2$ solution using 2 spray cycles. (b) Degradation curves of MB by as-deposited samples under UV-B illumination: NiO films (1, 2, and 4 spray cycles) on glass, ZnO_{NR} , and $\text{ZnO}_{\text{NR}}/\text{NiO}(1)$, $\text{ZnO}_{\text{NR}}/\text{NiO}(2)$, $\text{ZnO}_{\text{NR}}/\text{NiO}(4)$ core-shell heterostructures; NiO in $\text{ZnO}_{\text{NR}}/\text{NiO}(1)$, $\text{ZnO}_{\text{NR}}/\text{NiO}(2)$, and $\text{ZnO}_{\text{NR}}/\text{NiO}(4)$ was deposited at $T_s = 500^\circ\text{C}$ from 5 mM $\text{Ni}(\text{acac})_2$ in ethanol solution using 1, 2, and 4 spray cycles, respectively. (c) Reusability test of photodegradation of MB by ZnO_{NR} and the $\text{ZnO}_{\text{NR}}/\text{NiO}(2)$ core-shell heterostructure.

$\text{ZnO}_{\text{NR}}/\text{NiO}$ core-shell structure.

The MB photocatalytic degradation curves for the as-deposited $\text{ZnO}_{\text{NR}}/\text{NiO}$ core-shell heterostructures and their components, NiO films and ZnO_{NR} , are shown in Fig. 3b, and the corresponding degradation efficiencies and k values are summarized in Table 3.

Independent of the number of spray cycles, the NiO films showed a negligible degradation efficiency of ca. 1%. Compared to the ZnO film (Table 2), ZnO_{NR} showed nearly twice the MB degradation efficiency, with a value of 48% (Table 3), which can be explained by the higher active surface area of the nanorod layer but may also imply contributions from different surface chemical components [39]. Moreover, $\text{ZnO}_{\text{NR}}/\text{NiO}$ core-shell heterostructures with NiO thicknesses corresponding to 1 or 2 spray cycles exhibited degradation efficiencies of 60% and 64%, respectively, which were higher than the degradation efficiency of 48% obtained by bare ZnO_{NR} . A thicker NiO layer (corresponding to 4 spray cycles) in the $\text{ZnO}_{\text{NR}}/\text{NiO}$ core-shell heterostructure

Table 3

Degradation efficiencies of MB and degradation rate constants (k) by as-deposited samples and samples annealed at $T_{\text{an}} = 600^\circ\text{C}$ in air for 1 h: NiO films; ZnO nanorods (ZnO_{NR}); and $\text{ZnO}_{\text{NR}}/\text{NiO}$ core-shell heterostructures with NiO from 1, 2 and 4 spray cycles. NiO was deposited at $T_s = 500^\circ\text{C}$ from 5 mM $\text{Ni}(\text{acac})_2$ in ethanol solution.

Sample	Degradation efficiency (%)		$k \times 10^{-3} (\text{min}^{-1})$	
	As-dep	$T_{\text{an}} = 600^\circ\text{C}$	As-dep	$T_{\text{an}} = 600^\circ\text{C}$
NiO films	1	2	–	–
ZnO_{NR}	48	53	3.42	4.13
$\text{ZnO}_{\text{NR}}/\text{NiO}(1)$	60	65	5.01	5.66
$\text{ZnO}_{\text{NR}}/\text{NiO}(2)$	64	70	5.51	7.21
$\text{ZnO}_{\text{NR}}/\text{NiO}(4)$	44	50	2.91	3.77

significantly decreased the degradation efficiency from 64% to 44%, showing that it is extremely important to optimize the shell layer thickness.

Similar to the bilayers (Section 3.2), postdeposition annealing at 600°C was applied to the $\text{ZnO}_{\text{NR}}/\text{NiO}$ core-shell heterostructures. Annealing resulted in enhancement of MB degradation efficiency, as summarized in Table 3. For instance, the MB degradation efficiency by $\text{ZnO}_{\text{NR}}/\text{NiO}(2)$ increased from 64% to 70%. Thus, annealing is an important procedure to improve the material properties and quality of heterojunctions.

It is worth mentioning that several research groups have reported the advantages of core-shell heterostructure photocatalysts. Periyannan et al. [11] reported that a $\text{ZnO}_{\text{NR}}/\text{NiO}$ core-shell heterostructure obtained by sputtering NiO on hydrothermally grown ZnO_{NR} exhibited a rhodamine-B degradation efficiency of 58% under UV light in 3 h, in contrast to 54% for bare ZnO_{NR} . For an alternative $\text{ZnO}_{\text{NR}}/\text{Cu}_x\text{O}$ core-shell heterostructure, Montero et al. [10] showed a 65% degradation efficiency towards orange II dye under UV light in 3 h, in contrast to 55% for bare ZnO_{NR} .

The k values before and after annealing at 600°C are presented in Table 3. For the best-performing $\text{ZnO}_{\text{NR}}/\text{NiO}(2)$ sample, the k value of $7.21 \times 10^{-3} \text{ min}^{-1}$ was 1.7 times higher than that of bare ZnO_{NR} .

For practical applications, photocatalysts must be reliable and stable. Thus, a reusability test of MB photodegradation by ZnO_{NR} and the $\text{ZnO}_{\text{NR}}/\text{NiO}(2)$ core-shell heterostructure was performed, and the results are presented in Fig. 3c. The measurements were repeated ten times, and for each measurement point, three parallel samples were used. The results show high reproducibility and stability since both ZnO_{NR} and the $\text{ZnO}_{\text{NR}}/\text{NiO}(2)$ core-shell heterostructure still showed MB degradation efficiencies of ca. 44–50% and ca. 61–66%, which are comparable to the initial values.

3.4. XPS analysis of ZnO_{NR}/NiO core-shell heterostructures

XPS analysis was applied to prove the presence of NiO on the surface of ZnO_{NR} and to gain an understanding of the surface chemical composition of ZnO_{NR}-600, ZnO_{NR}/NiO(2)-600, and ZnO_{NR}/NiO(4)-600. The Zn 2p_{3/2}, Ni 2p, and O 1s core-level spectra of these samples are presented in Fig. 4(a), (b), and (c), respectively. The binding energy (BE) of Zn 2p_{3/2} of ZnO_{NR}-600 was centered at 1020.7 eV (Fig. 4a), corresponding to the reported BE value of Zn 2p_{3/2} from ZnO [40,41]. Compared to the result for ZnO_{NR}-600, the Zn 2p_{3/2} peak intensity was significantly decreased for the samples where NiO was deposited onto ZnO_{NR} using two (ZnO_{NR}/NiO(2)-600) or four spray cycles (ZnO_{NR}/NiO(4)-600). The peaks at BEs of 852.5 ± 0.3 eV and 870.9 ± 0.3 eV in the spectra of ZnO_{NR}/NiO(2)-600 and ZnO_{NR}/NiO(4)-600 are commonly assigned to Ni 2p_{3/2} and Ni 2p_{1/2} of NiO, respectively (Fig. 4b) [20]. The XPS spectra also confirmed that NiO was present on the surface of ZnO_{NR}, although NiO was not detected by XRD due to the low film thickness and can hardly be seen in the SEM image (Fig. 2a).

In the analysis of the O1s spectra of ZnO_{NR}-600, the best fit was achieved involving three peaks positioned at BEs of 530.2 eV, 531.8 eV and 532.9 eV, assigned to Zn-O bonds, surface hydroxyl groups (OH⁻), and surface H₂O, respectively [33,39,42]. After covering the nanorods with NiO, a new contribution in the O 1s spectra was revealed at a BE of 528.8 ± 0.1 eV, characteristic of Ni-O bonds [20,43].

It is worth noting that for the ZnO_{NR}/NiO(2)-600 and ZnO_{NR}/NiO(4)-600 heterostructures, the BE of Zn 2p_{3/2} shifted by 0.9 eV and 1.1 eV, respectively, towards lower values compared to the BE of Zn 2p_{3/2} of ZnO_{NR}-600, positioned at 1020.7 eV (Fig. 4a, Table 4). Different reports can be found in the literature about the shift in the BE of Zn 2p emission as a result of ZnO coating with NiO forming a heterostructure. A similar shift in Zn 2p_{3/2} to a lower BE was observed for the ZnO_{NR}/NiO core-shell heterostructure prepared by Periyannan et al. [11]. In that study, a Zn 2p_{3/2} peak shift of 1.1 eV to lower BE values compared to that in pristine ZnO_{NR} was detected. In contrast, Tian et al. [44] reported that for a ZnO/NiO nanocomposite, the Zn 2p_{3/2} BE shifted by 0.6 eV to

a higher energy compared to that of ZnO. Zhang et al. [26] also observed a Zn 2p_{3/2} BE shift of 0.9 eV to a higher energy for a ZnO/NiO nanofiber structure compared to the corresponding value for ZnO nanofibers. Although ZnO/NiO heterostructures were characterized in all these studies, the obtained results are contradictory to some extent. Our results seem to support those reported by Periyannan et al. [11] rather than those reported by Tian et al. [44] and Zhang et al. [26].

To gain more clarity, the Zn_{LMM} Auger spectra of ZnO_{NR}-600, ZnO_{NR}/NiO(2)-600 and ZnO_{NR}/NiO(4)-600 were analyzed. The kinetic energy of Zn_{LMM} and Auger parameter results are presented in Table 4.

The most striking result of this analysis is the observation of a 1.9–2.0 eV difference between the modified Auger parameter values of pristine ZnO_{NR} and ZnO_{NR}/NiO heterostructures. Although the aforementioned BE shift observed by XPS has been related to the formation of heterojunctions, the changes in the Auger parameter confirm the existence of a built-in electric field at the heterojunction interface.

3.5. Band diagram of the ZnO_{NR}/NiO core-shell heterostructure and MB degradation mechanism

To understand the mechanism of photocatalytic degradation by ZnO_{NR}/NiO core-shell heterojunctions, the energetic diagram was evaluated by combining KP and PYS analysis data. The work functions of ZnO_{NR}-600 and ZnO_{NR}/NiO(2)-600 were measured in the dark, and the results are presented in Fig. 5a. The measured work functions of ZnO_{NR}-600 and ZnO_{NR}/NiO(2)-600 showed constant mean values within standard deviations of ± 2 meV, indicating stable surface electronic properties related to the surface chemical stability [35]. The work function was 4.42 eV for ZnO_{NR}-600 and 4.70 eV for ZnO_{NR}/NiO(2)-600. The higher work function value for ZnO_{NR}/NiO(2)-600 than ZnO_{NR}-600 proves the presence of the NiO thin film on the surface of ZnO_{NR}.

The ionization energy (E_i) of ZnO_{NR}-600 and ZnO_{NR}/NiO(2)-600 was measured by PYS. The PYS spectra are presented in Fig. 5b and c, respectively, and the E_i values are summarized in Table 5. The ionization energy is 6.29 eV for ZnO_{NR}-600 and 5.40 eV for ZnO_{NR}/NiO(2)-600. To draw the band diagram of the ZnO_{NR}/NiO heterojunction, the valence band maximum (E_{VBM}) relative to the Fermi level (E_F) was calculated as the difference between the work function (Φ) and ionization energy (E_i), $E_{VBM} = \Phi - E_i$, since Φ defines the E_F position relative to the local vacuum level and E_i is measured relative to the same local vacuum level. [35]. The conduction band minimum (CBM) was calculated as $E_{CBM} = E_{VBM} + E_g$ by using the bandgaps of the hydrothermally grown ZnO_{NR} (3.27 eV) [33] and USP-grown NiO (3.70 eV, Table 1). With the known VBM and CBM positions, the energy band diagram of the ZnO_{NR}/NiO heterostructure could be drawn as shown in Fig. 5d. Thus, the energy band diagram shows n-type conductivity for ZnO_{NR} and p-type conductivity for the NiO film, which agrees with the results of the hot probe measurements in Section 3.2. In addition, rectifying current-voltage behavior is predicted.

It is worth mentioning that in most PA studies, the formation of ZnO/NiO heterojunctions is proposed based on PA results rather than relying on the real energetic parameters of the heterostructure [8,13,18,23,25]. For instance, Thampy et al. [18] claimed that the increased MB degradation efficiency by ZnO/NiO nanoparticles is due to the formation of ZnO/NiO heterojunctions. Additionally, Hameed et al. [8] compared only the MB degradation efficiencies obtained with ZnO/NiO nanoparticles and their single components and concluded that ZnO/NiO heterojunction formation was responsible for the difference. Tian et al. [13] and Liu et al. [25] studied the degradation of methyl orange by ZnO/NiO particles and similarly concluded that the formation of a ZnO/NiO heterojunction was responsible, based only on the PA results. The band diagram was drawn based on compiled parameters from the literature [13,18,23,25]. However, none of the abovementioned studies provided experimentally measured energetic parameters. Thus, the

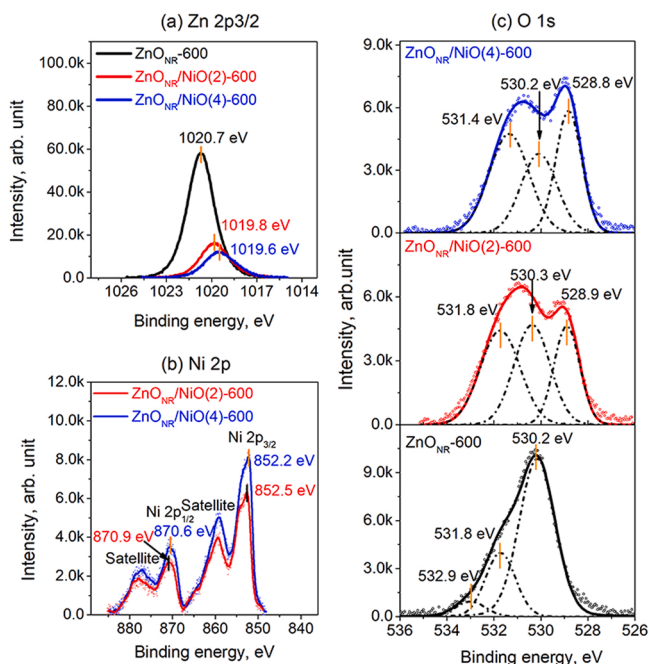


Fig. 4. XPS core-level spectra from ZnO_{NR}-600, ZnO_{NR}/NiO(2)-600, and ZnO_{NR}/NiO(4)-600: (a) Zn 2p_{3/2}, (b) Ni 2p, (c) O 1s. NiO in ZnO_{NR}/NiO(2)-600 and ZnO_{NR}/NiO(4)-600 was deposited at $T_s = 500$ °C from 5 mM Ni(acac)₂ in ethanol solution using 2 and 4 spray cycles, respectively. All the samples were annealed at 600 °C for 1 h in air.

Table 4

Binding energy (BE) of the O 1s, Ni 2p, Zn 2p_{3/2} core levels, kinetic energy of Zn_{LMM}, and the modified Auger parameter (α') for ZnO_{NR}-600, ZnO_{NR}/NiO(2)-600, and ZnO_{NR}/NiO(4)-600. NiO in ZnO_{NR}/NiO(2)-600 and ZnO_{NR}/NiO(4)-600 was deposited at $T_s = 500$ °C from 5 mM Ni(acac)₂ in ethanol solution using 2 and 4 spray cycles, respectively. All the samples were annealed at 600 °C for 1 h in air.

Sample name	BE (eV)							KE (eV)	α' (eV)
	O 1s				Ni 2p _{3/2}	Ni 2p _{1/2}	Zn 2p _{3/2}		
	ZnO	OH	H ₂ O	NiO					
ZnO _{NR} -600	530.2	531.8	532.9	–	–	–	1020.7	988.5	2009.2
ZnO _{NR} /NiO(2)-600	530.3	531.8	–	528.9	852.5	870.9	1019.8	987.4	2007.2
ZnO _{NR} /NiO(4)-600	530.2	531.4	–	528.8	852.2	870.6	1019.6	987.9	2007.3

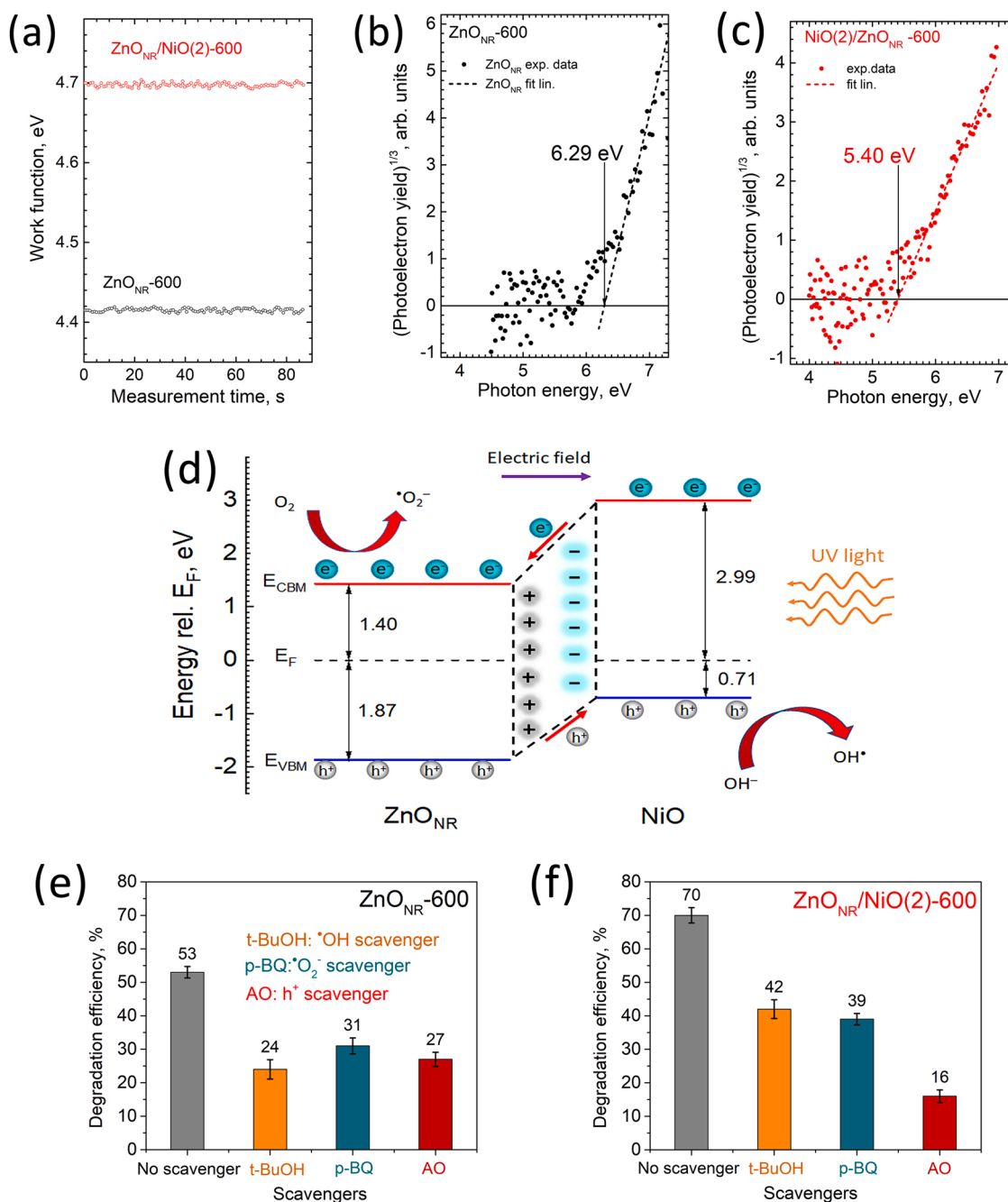


Fig. 5. (a) Time-dependent work function of ZnO_{NR}-600 and ZnO_{NR}/NiO(2)-600. (b) Photoelectron yield spectrum of ZnO_{NR}-600. (c) Photoelectron yield spectrum of ZnO_{NR}/NiO(2)-600. (d) Energy band diagram of ZnO_{NR}/NiO heterojunction. (e) Influence of [•]OH, [•]O₂⁻ and h⁺ scavengers on the MB degradation efficiency by ZnO_{NR}-600. (f) Influence of [•]OH, [•]O₂⁻ and h⁺ scavengers on the MB degradation efficiency by ZnO_{NR}/NiO(2)-600. NiO in ZnO_{NR}/NiO(2) heterostructure was deposited at $T_s = 500$ °C from 5 mM Ni(acac)₂ in ethanol solution using 2 spray cycles. All the samples were annealed at $T_{an} = 600$ °C for 1 h in air.

Table 5

Work function (Φ), ionization energy (E_i) and the energy difference between the Fermi level (E_F) and valence band maximum (E_{VBM}) of ZnO_{NR}-600 and ZnO_{NR}/NiO(2)-600. NiO was deposited at $T_d = 500$ °C from 5 mM Ni(acac)₂ in ethanol solution using 2 spray cycles. Both samples were annealed at 600 °C for 1 h in air.

Sample	Φ (± 0.04 eV)	E_i (± 0.03 eV)	$E_F - E_{VBM}$ (± 0.05 eV)
ZnO _{NR} -600	4.42	6.29	-1.87
ZnO _{NR} /NiO(2)-600	4.70	5.41	-0.71

band diagram of the ZnO_{NR}/NiO heterojunction based on directly measured experimental data (Fig. 5d) and the photocatalytic degradation mechanism was proposed here.

Following the classical concept of heterojunction formation [45], electrons transfer from ZnO to NiO and holes transfer from NiO to ZnO until the system reaches thermodynamic equilibrium and an inner electric field forms at the heterointerface. When the ZnO/NiO heterostructure is irradiated by UV light, electron-hole pairs are generated in both ZnO and NiO, and electrons from the valence band (VB) can be excited to the conduction band (CB) in both materials with the simultaneous formation of the same number of holes in the VB. However, our experimentally proven band alignment for the p-NiO/n-ZnO heterojunction (Fig. 5d) supports the transfer of photogenerated electrons from the CB of NiO to the CB of ZnO and the transfer of photogenerated holes from the VB of ZnO to the VB of NiO, indicating that the electrons and holes are efficiently separated. The electrons from ZnO and holes from NiO are injected into the reaction medium and participate in chemical reactions to degrade different organic pollutants. The electrons interact with dissolved O₂ molecules and produce superoxide radical ($\cdot\text{O}_2^-$). The photogenerated holes are trapped by OH⁻, forming hydroxyl radical species ($\cdot\text{OH}$).

To verify the role of $\cdot\text{OH}$, $\cdot\text{O}_2^-$ and h^+ in the photodegradation process, MB photodegradation measurements were performed in the presence of different scavengers (such as tert-Butanol as $\cdot\text{OH}$ scavenger, p-Benzoquinone as $\cdot\text{O}_2^-$ scavenger, and ammonium oxalate as h^+ scavenger). The results of the test are presented in Fig. 5e and f. Both ZnO_{NR}-600 and ZnO_{NR}/NiO(2)-600 exhibited lower degradation efficiency of MB in the presence of $\cdot\text{OH}$, $\cdot\text{O}_2^-$ and h^+ scavengers compared to that measured without adding a scavenger, indicating the active role $\cdot\text{OH}$ and $\cdot\text{O}_2^-$ species, as well as the role of the photogenerated carriers responsible for the generation of related radicals. The impact of the latest one is well supported by the enhanced photocatalytic activity of ZnO_{NR}/NiO heterojunction (compared to ZnO_{NR} alone, Fig. 5e) in which the photogenerated carriers are efficiently separated towards the surface and transferred to reactive surface sites. The reduced degradation efficiency of MB by ZnO_{NR}/NiO(2)-600 in the presence of the ammonium oxalate as h^+ scavenger (Fig. 5f) suggests that the photogenerated holes are efficiently transferred towards the surface of NiO shell contributing to the degradation efficiency of MB through the formation of $\cdot\text{OH}$ radicals.

This study clearly demonstrated that the efficient separation of charge carriers at the ZnO_{NR}/NiO heterointerface boosts the photocatalytic performance.

4. Conclusions

In this study, we demonstrated for the first time that homogeneous crystalline films of NiO with cubic structure can be successfully grown on glass substrates by employing a robust ultrasonic spray technique and nickel acetylacetonate as a source material. Increasing the deposition temperature from 350 to 500 °C increased the NiO film thickness from ca. 30 to ca. 70 nm, and the mean crystallite size increased from ca. 17 to ca. 30 nm. Post-deposition annealing of as-grown films at 600 °C in air slightly increased the mean crystallite size. The films exhibited a direct

bandgap value of 3.7 eV after annealing.

NiO layers were applied to ZnO films and ZnO nanorods to fabricate ZnO/NiO bilayer and ZnO_{NR}/NiO core-shell heterostructures for which optimal preparation temperature and thickness were found. The photocatalytic degradation of MB by the NiO film, ZnO film, ZnO_{NR}, ZnO/NiO bilayer, and ZnO_{NR}/NiO core-shell heterostructure was analyzed under ultraviolet irradiation for 180 min. While the ZnO_{NR} showed a reasonable degradation efficiency of 48 %, NiO alone exhibited a negligible performance of 1–2 %. The record degradation efficiency of 70 % was achieved by ZnO_{NR}/NiO core-shell heterostructure, with optimized NiO shell thickness from two spray cycles, deposition temperature of 500 °C, and post-deposition air treatment at 600 °C.

Current-voltage characteristics of ZnO/NiO bilayer indicate the formation of rectifying behavior between n-type ZnO and p-type NiO film, being an approval of p-n junction formation. XPS analysis confirmed the formation of NiO shell on ZnO core and showed a 1.9–2.0 eV difference in modified Auger parameter between ZnO_{NR} and ZnO_{NR}/NiO core-shell heterostructure, validating the presence of built-in electric field at the interface. A type-II band diagram between NiO and ZnO_{NR} is proposed based on Kelvin probe and photoelectron yield spectroscopy measurements. Based on these results, the degradation mechanism of MB is discussed in which the built-in electric field at the heterointerface stimulated the enhanced photocatalytic activity.

To our knowledge, the achieved photocatalytic activity is the highest reported for the degradation of MB, employing ZnO_{NR}/NiO core-shell heterojunction concept. A similar ZnO_{NR}/NiO core-shell heterojunction photocatalyst was applied in one recent study [11], however, the degradation efficiency of 58 % was reported for a Rhodamine B pollutant. Our study provides an advanced and feasible proof of concept design for cost-effective heterojunction photocatalysts. Further research efforts on optimization of the related material and interfaces will allow subsequent improvement of photocatalytic activity and deployment of the device for wider range of pollutants.

CRedit authorship contribution statement

Zengjun Chen: Conceptualization, Formal analysis, Methodology, Software, Writing – original draft. **Tatjana Dedova:** Methodology, Supervision, Writing – review & editing. **Nicolae Spalatu:** Methodology, Formal analysis, Writing – review & editing. **Natalia Maticiu:** Formal analysis, Writing – review & editing. **Marin Rusu:** Formal analysis, Writing – review & editing. **Atanas Katerski:** Formal analysis, Writing – review & editing. **Ilona Oja Acik:** Project administration, Funding acquisition, Writing – review & editing. **Thomas Unold:** Writing – review & editing. **Malle Krunks:** Conceptualization, Methodology, Funding acquisition, Supervision, Writing – review & editing.

Declaration of Competing Interest

The authors declare that they have no known competing financial interests or personal relationships that could have appeared to influence the work reported in this paper.

Acknowledgement

This study was funded by the Estonian Research Council (project PRG627), the Archimedes SA (Estonian Centre of Excellence Project TK141 (TAR16016EK)), the European Commission's H2020 programme under the ERA Chair (grant agreement No 952509), and the ASTRA "TUT Institutional Development Programme for 2016–2022" Graduate School of Functional Materials and Technologies (2014–2020.4.01.16-0032).

Appendix A. Supporting information

Supplementary data associated with this article can be found in the

online version at [doi:10.1016/j.colsurfa.2022.129366](https://doi.org/10.1016/j.colsurfa.2022.129366).

References

- U.I. Gaya, A.H. Abdullah, Heterogeneous photocatalytic degradation of organic contaminants over titanium dioxide: a review of fundamentals, progress and problems, *J. Photochem. Photobiol. C Photochem. Rev.* 9 (1) (2008) 1–12, <https://doi.org/10.1016/j.jphotochemrev.2007.12.003>.
- K. Qi, B. Cheng, J. Yu, W. Ho, Review on the improvement of the photocatalytic and antibacterial activities of ZnO, *J. Alloy. Compd.* 727 (2017) 792–820, <https://doi.org/10.1016/j.jallcom.2017.08.142>.
- F. Liu, M.Y. Guo, Y.H. Leung, A.B. Djurišić, A.M.C. Ng, W.K. Chan, Effect of starting properties and annealing on photocatalytic activity of ZnO nanoparticles, *Appl. Surf. Sci.* 283 (2013) 914–923, <https://doi.org/10.1016/j.apsusc.2013.07.043>.
- M.Y. Guo, A.M.C. Ng, F. Liu, A.B. Djurišić, W.K. Chan, H. Su, K.S. Wong, Effect of native defects on photocatalytic properties of ZnO, *J. Phys. Chem. C* 115 (22) (2011) 11095–11101, <https://doi.org/10.1021/jp200926u>.
- T. Varadavenkatesan, E. Lyubchik, S. Pai, A. Pugazhendhi, R. Vinayagam, R. Selvaraj, Photocatalytic degradation of Rhodamine B by zinc oxide nanoparticles synthesized using the leaf extract of *Cyanometra ramiflora*, *J. Photochem. Photobiol. B Biol.* 199 (2019), 111621, <https://doi.org/10.1016/j.jphotobiol.2019.111621>.
- A. Umar, M.S. Akhtar, A. Al-Hajry, M.S. Al-Assiri, G.N. Dar, M. Saif Islam, Enhanced photocatalytic degradation of harmful dye and phenyl hydrazine chemical sensing using ZnO nanorods, *Chem. Eng. J.* 262 (2015) 588–596, <https://doi.org/10.1016/j.cej.2014.09.111>.
- D. Lei, J. Xue, Q. Bi, C. Tang, L. Zhang, 3D/2D direct Z-scheme photocatalyst Zn₂SnO₄/CdS for simultaneous removal of Cr(VI) and organic pollutant, *Appl. Surf. Sci.* 517 (2020), 146030, <https://doi.org/10.1016/j.apsusc.2020.146030>.
- A. Hameed, T. Montini, V. Gombac, P. Fornasiero, Photocatalytic decolorization of dyes on NiO–ZnO nano-composites, *Photochem. Photobiol. Sci.* 8 (5) (2009) 677–682, <https://doi.org/10.1039/B817396F>.
- S. Balachandran, M. Swaminathan, Facile fabrication of heterostructured Bi₂O₃–ZnO photocatalyst and its enhanced photocatalytic activity, *J. Phys. Chem. C* 116 (5) (2012) 26306–26312, <https://doi.org/10.1021/jp306874z>.
- J. Montero, T. Welearegay, J. Thyrr, H. Stopfel, T. Dedova, I.O. Acik, L. Österlund, Copper–zinc oxide heterojunction catalysts exhibiting enhanced photocatalytic activity prepared by a hybrid deposition method, *RSC Adv.* 11 (17) (2021) 10224–10234, <https://doi.org/10.1039/D1RA00691F>.
- S. Periyannan, L. Mancieru, N.D. Nguyen, A. Klein, W. Jaegermann, P. Colson, C. Henrist, R. Cloots, Influence of ZnO surface modification on the photocatalytic performance of ZnO/NiO thin films, *Catal. Lett.* 149 (7) (2019) 1813–1824, <https://doi.org/10.1007/s10562-019-02781-z>.
- M. Ding, H. Yang, T. Yan, C. Wang, X. Deng, S. Zhang, J. Huang, M. Shao, X. Xu, Fabrication of hierarchical ZnO@NiO core–shell heterostructures for improved photocatalytic performance, *Nanoscale Res. Lett.* 13 (1) (2018) 260, <https://doi.org/10.1186/s11671-018-2676-1>.
- F. Tian, Y. Liu, Synthesis of p-type NiO/n-type ZnO heterostructure and its enhanced photocatalytic activity, *Scr. Mater.* 69 (5) (2013) 417–419, <https://doi.org/10.1016/j.scriptamat.2013.05.040>.
- M. Wang, Y. Hu, J. Han, R. Guo, H. Xiong, Y. Yin, TiO₂/NiO hybrid shells: p–n junction photocatalysts with enhanced activity under visible light, *J. Mater. Chem. A* 3 (41) (2015) 20727–20735, <https://doi.org/10.1039/C5TA05839B>.
- P. Nandi, D. Das, ZnO–Cu₂O heterostructure photocatalyst for efficient dye degradation, *J. Phys. Chem. Solids* 143 (2020), 109463, <https://doi.org/10.1016/j.jpcs.2020.109463>.
- C. Liu, F. Meng, L. Zhang, D. Zhang, S. Wei, K. Qi, J. Fan, H. Zhang, X. Cui, CuO/ZnO heterojunction nanoarrays for enhanced photoelectrochemical water oxidation, *Appl. Surf. Sci.* 469 (2019) 276–282, <https://doi.org/10.1016/j.apsusc.2018.11.054>.
- J. Yu, S. Zhuang, X. Xu, W. Zhu, B. Feng, J. Hu, Photogenerated electron reservoir in hetero-p–n CuO–ZnO nanocomposite device for visible-light-driven photocatalytic reduction of aqueous Cr(VI), *J. Mater. Chem. A* 3 (3) (2015) 1199–1207, <https://doi.org/10.1039/C4TA04526B>.
- U.S.U. Thampy, A. Mahesh, K.S. Sibi, I.N. Jawahar, V. Biju, Enhanced photocatalytic activity of ZnO–NiO nanocomposites synthesized through a facile sonochemical route, *Sn Appl. Sci.* 1 (11) (2019) 15, <https://doi.org/10.1007/s42452-019-1426-z>.
- M. Xiao, Y. Lu, Y. Li, H. Song, L. Zhu, Z. Ye, A new type of p-type NiO/n-type ZnO nano-heterojunctions with enhanced photocatalytic activity, *RSC Adv.* 4 (65) (2014) 34649–34653, <https://doi.org/10.1039/C4RA04600E>.
- Z. Chen, T. Dedova, I.O. Acik, M. Danilson, M. Krunks, Nickel oxide films by chemical spray: effect of deposition temperature and solvent type on structural, optical, and surface properties, *Appl. Surf. Sci.* 548 (2021), 149118, <https://doi.org/10.1016/j.apsusc.2021.149118>.
- A.A. Al-Ghamdi, M.S. Abdel-wahab, A.A. Farghali, P.M.Z. Hasan, Structural, optical and photo-catalytic activity of nanocrystalline NiO thin films, *Mater. Res. Bull.* 75 (2016) 71–77, <https://doi.org/10.1016/j.materresbull.2015.11.027>.
- K.O. Ukoba, A.C. Eloka-Eboka, F.L. Inambao, Review of nanostructured NiO thin film deposition using the spray pyrolysis technique, *Renew. Sustain. Energy Rev.* 82 (2018) 2900–2915, <https://doi.org/10.1016/j.rser.2017.10.041>.
- H. Derikvand, A. Nezamzadeh-Ejhihi, Increased photocatalytic activity of NiO and ZnO in photodegradation of a model drug aqueous solution: effect of coupling, supporting, particles size and calcination temperature, *J. Hazard. Mater.* 321 (2017) 629–638, <https://doi.org/10.1016/j.jhazmat.2016.09.056>.
- M.M. Sabzehmeidani, H. Karimi, M. Ghaedi, Electrospinning preparation of NiO/ZnO composite nanofibers for photodegradation of binary mixture of rhodamine B and methylene blue in aqueous solution: central composite optimization, *Appl. Organomet. Chem.* 32 (6) (2018), <https://doi.org/10.1002/aoc.4335>.
- Y. Liu, G. Li, R. Mi, C. Deng, P. Gao, An environment-benign method for the synthesis of p-NiO/n-ZnO heterostructure with excellent performance for gas sensing and photocatalysis, *Sens. Actuators B Chem.* 191 (2014) 537–544, <https://doi.org/10.1016/j.snb.2013.10.068>.
- Z. Zhang, C. Shao, X. Li, C. Wang, M. Zhang, Y. Liu, Electrospun nanofibers of p-type NiO/n-type ZnO heterojunctions with enhanced photocatalytic activity, *ACS Appl. Mater. Interfaces* 2 (10) (2010) 2915–2923, <https://doi.org/10.1021/am100618h>.
- J.H. Huang, J.X. Chen, Y.F. Tu, Y. Tian, D. Zhou, G. Zheng, J.P. Sang, Q.M. Fu, Preparation and photocatalytic activity of CuO/ZnO composite nanostructured films, *Mater. Res. Express* 6 (1) (2019), <https://doi.org/10.1088/2053-1591/aa66ff>.
- W. Jing, W. Gao, Z. Li, M. Peng, F. Han, Z. Wei, Z. Yang, Z. Jiang, Regulation of the volume flow rate of aqueous methyl blue solution and the wettability of CuO/ZnO nanorods to improve the photodegradation performance of related microfluidic reactors, *Langmuir* 37 (26) (2021) 7890–7906, <https://doi.org/10.1021/acs.langmuir.1c00407>.
- I. Dundar, M. Krivevskaya, A. Katerski, I.O. Acik, TiO₂ thin films by ultrasonic spray pyrolysis as photocatalytic material for air purification, *R. Soc. Open Sci.* 6 (2) (2019), <https://doi.org/10.1098/rsos.181578>.
- R. Parize, A. Katerski, I. Gromyko, L. Rapenne, H. Roussel, E. Kärber, E. Appert, M. Krunks, V. Consonni, ZnO/TiO₂/Sb₂S₃ core–shell nanowire heterostructure for extremely thin absorber solar cells, *J. Phys. Chem. C* 121 (18) (2017) 9672–9680, <https://doi.org/10.1021/acs.jpcc.7b00178>.
- A.T. Oluwabi, A. Katerski, E. Carlos, R. Branquinho, A. Mere, M. Krunks, E. Fortunato, L. Pereira, I. Oja Acik, Application of ultrasonic spray pyrolysis zinc tin oxide-based thin film transistor, *J. Mater. Chem. C* 8 (11) (2020) 3730–3739, <https://doi.org/10.1039/C9TC05127A>.
- X.H. Chan, J.R. Jennings, M.A. Hossain, K.K.Z. Yu, Q. Wang, Characteristics of p-NiO thin films prepared by spray pyrolysis and their application in CdS-sensitized photocathodes, *J. Electrochem. Soc.* 158 (7) (2011) H733–H740, <https://doi.org/10.1149/1.3590742>.
- T. Dedova, I.O. Acik, Z. Chen, A. Katerski, K. Balmassov, I. Gromyko, T. Nagyné-Kovács, I.M. Szilágyi, M. Krunks, Enhanced photocatalytic activity of ZnO nanorods by surface treatment with HAuCl₄: Synergic effects through an electron scavenging, plasmon resonance and surface hydroxylation, *Mater. Chem. Phys.* 245 (2020), 122767, <https://doi.org/10.1016/j.matchemphys.2020.122767>.
- N. Maticiuc, T. Kodalle, J. Lauche, R. Wenisch, T. Bertram, C.A. Kaufmann, I. Lauermann, In vacuo XPS investigation of Cu(In,Ga)Se₂ surface after RbF post-deposition treatment, *Thin Solid Films* 665 (2018) 143–147, <https://doi.org/10.1016/j.tsf.2018.09.026>.
- M. Rusu, T. Kodalle, L. Choubrac, N. Barreau, C.A. Kaufmann, R. Schlattmann, T. Unold, Electronic structure of the CdS/Cu(In,Ga)Se₂ interface of KF- and RbF-treated samples by Kelvin Probe and photoelectron yield spectroscopy, *ACS Appl. Mater. Interfaces* 13 (6) (2021) 7745–7755, <https://doi.org/10.1021/acsaami.0c20976>.
- X. Chen, Z. Wu, D. Liu, Z. Gao, Preparation of ZnO photocatalyst for the efficient and rapid photocatalytic degradation of Azo Dyes, 143–143, *Nanoscale Res. Lett.* 12 (1) (2017), <https://doi.org/10.1186/s11671-017-1904-4>.
- I. Oja, A. Mere, M. Krunks, R. Nisumaa, C.H. Solterbeck, M. Es-Souani, Structural and electrical characterization of TiO₂ films grown by spray pyrolysis, *Thin Solid Films* 515 (2) (2006) 674–677, <https://doi.org/10.1016/j.tsf.2005.12.243>.
- D. Ao, Z. Li, Y. Fu, Y. Tang, S. Yan, X. Zu, Heterostructured NiO/ZnO nanorod arrays with significantly enhanced H₂S sensing performance, *Nanomaterials* 9 (6) (2019) 900, <https://doi.org/10.3390/nano9060900>.
- I. Gromyko, M. Krunks, T. Dedova, A. Katerski, D. Klauson, I. Oja Acik, Surface properties of sprayed and electrodeposited ZnO rod layers, *Appl. Surf. Sci.* 405 (2017) 521–528, <https://doi.org/10.1016/j.apsusc.2017.02.065>.
- A. Pal, T.K. Dey, A. Singhal, R.C. Bindal, P.K. Tewari, Nano-ZnO impregnated inorganic-polymer hybrid thinfilm nanocomposite nanofiltration membranes: an investigation of variation in structure, morphology and transport properties, *RSC Adv.* 5 (43) (2015) 34134–34151, <https://doi.org/10.1039/c4ra14854a>.
- M. Wang, L. Jiang, E.J. Kim, S.H. Hahn, Electronic structure and optical properties of Zn(OH)₂: LDA+U calculations and intense yellow luminescence, *RSC Adv.* 5 (106) (2015) 87496–87503, <https://doi.org/10.1039/C5RA17024A>.
- R. Al-Gaashani, S. Radiman, A.R. Daud, N. Tabet, Y. Al-Douri, XPS and optical studies of different morphologies of ZnO nanostructures prepared by microwave methods, *Ceram. Int.* 39 (3) (2013) 2283–2292, <https://doi.org/10.1016/j.ceramint.2012.08.075>.
- K. Sakamoto, F. Hayashi, K. Sato, M. Hirano, N. Ohtsu, XPS spectral analysis for a multiple oxide comprising NiO, TiO₂, and NiTiO₃, *Appl. Surf. Sci.* 526 (2020), 146729, <https://doi.org/10.1016/j.apsusc.2020.146729>.
- H. Tian, H. Fan, G. Dong, L. Ma, J. Ma, NiO/ZnO p–n heterostructures and their gas sensing properties for reduced operating temperature, *RSC Adv.* 6 (110) (2016) 109091–109098, <https://doi.org/10.1039/C6RA19520B>.
- N. Spalatu, R. Krautmann, A. Katerski, E. Karber, R. Josepson, J. Hiie, I.O. Acik, M. Krunks, Screening and optimization of processing temperature for Sb₂Se₃ thin film growth protocol: Interrelation between grain structure, interface intermixing and solar cell performance, *Sol. Energy Mater. Sol. Cells* 225 (2021), 111045, <https://doi.org/10.1016/j.solmat.2021.111045>.